ELSEVIER

International Journal of Refractory Metals & Hard Materials 19 (2001) 467–477

International Journal of REFRACTORY METALS & HARD MATERIALS

www.elsevier.com/locate/ijrmhm

Structure and high-temperature stability of compositionally graded CVD mullite coatings

Ping Hou, S.N. Basu *, V.K. Sarin

Department of Manufacturing Engineering, College of Engineering, Boston University, 15 St. Mary's Street, Boston, MA 02215, USA

Received 5 March 2001; accepted 18 July 2001

Abstract

Dense, uniform and crack-free mullite ($3Al_2O_3 \cdot 2SiO_2$) coatings were deposited on SiC by chemical vapor deposition. The coatings were compositionally graded, with the Al/Si ratio increasing towards the outer surface of the coatings for improved corrosion resistance. The coatings were found to start out as a nanocrystalline layer, which is an intimate mixture of γ-Al_2O_3 nanocrystallites imbedded in a vitreous silica-rich matrix at the substrate/coating interface. Mullite grains nucleated when the surface composition of the growing coating was in a narrow range close to that of stoichiometric mullite. The phase transformations occurring in these coatings during high-temperature anneals in the range 1100–1400 °C were studied. These phase transformations, which include a tetragonal-to-orthorhombic transformation, mullitization and devitrification of silica in the nanocrystalline layer, and α-alumina precipitation and twinning of the alumina-rich mullite, are discussed in light of the adhesion and corrosion resistance of the coatings.

Keywords: Mullite coatings; Chemical vapor deposition; Composition gradation; High-temperature stability

1. Introduction

The power generation and chemical industries require high performance materials that can withstand corrosive environments at elevated temperatures [1]. Due to their high-temperature strength, oxidation resistance, low creep rate and coefficient of thermal expansion (CTE), silicon-based ceramics such as SiC and Si_3N_4 have long been regarded as leading candidates for such applications, which include turbine blades, valves, piston heads, and heat exchangers [2–4]. Although Si-based ceramics form protective silica scales when exposed to oxygen-containing environments at elevated temperatures [5], the presence of species such as sulfur, chlorine and water vapor in the atmosphere can compromise this protective oxide scale, leading to an accelerated attack of the substrate [6–8]. The Si-based ceramics are also susceptible to severe degradation by hot-corrosion in the presence of molten Na_2SO_4 [9].

A practical approach of solving the problem of hot-corrosion is to deposit a protective coating on these Si-based materials when they are used in hostile environments. Mullite ($3Al_2O_3 \cdot 2SiO_2$) is an important engineering ceramic, which has excellent high-temperature strength and chemical stability at temperatures as high as 1500 °C [10]. In addition, mullite has low thermal conductivity as well as a close CTE match with the Si-based ceramics, especially with SiC (5.05×10^{-6} for mullite and 4.7×10^{-6} for SiC). This makes mullite a strong candidate material for corrosion-resistant coatings on Si-based ceramics [11].

2. Experimental details

Mullite coatings were deposited on polished bars of $3 \times 4 \times 20$ mm^3 Hexaloy SiC (Carborundum, Niagara Falls, NY). The coatings were deposited using the $AlCl_3$–$SiCl_4$–CO_2–H_2 system in a hot-wall chemical vapor deposition (CVD) reactor [12], with the overall reaction

$$6AlCl_3 + 2SiCl_4 + 13CO_2 + 13H_2 \leftrightarrow 3Al_2O_3 \cdot 2SiO_2 + 13CO + 26HCl$$

* Corresponding author. Tel.: +1-617-353-6728; fax: +1-617-353-5548.

E-mail address: basu@bu.edu (S.N. Basu).

0263-4368/01/$ - see front matter
PII: S0263-4368(01)00048-8

The $AlCl_3$ was formed in situ by flowing Cl_2 with Ar as a carrier gas, through heated Al chips, while $SiCl_4$ vapor was formed by evaporating liquid $SiCl_4$ at room temperature. The H_2 and CO_2 gases were mixed with the $AlCl_3$ and $SiCl_4$ prior to entry into the reaction chamber. The depositions were carried out at 950 °C and a total pressure of 75 Torr, with typical deposition rates of ~5 μm/h. The details of the coating deposition procedure are presented elsewhere [13].

To investigate the structural evolution of the as-deposited coatings at elevated temperatures, annealing experiments were conducted. Mullite-coated SiC samples were placed in alumina boats and annealed in air at atmospheric pressure. To study the resistance of the mullite coatings to thermal shock, samples were subjected to a cyclic oxidation test at 1250 °C. This test consisted of 500 cycles, with each cycle being an exposure of 1 h at 1250 °C and 1 h at room temperature with rapid heating and cooling between temperatures.

The coatings were examined by X-ray diffraction (XRD) for phase identification, using monochromatic $Cu_{K\alpha}$ radiation and a 0.02° step size with a 2.0 s dwell time. The surface and cross-section morphologies of the coatings were examined by a JEOL6100 scanning electron microscope (SEM), while electron transparent cross-sections were examined in a JEOL 2010FX transmission electron microscope (TEM). The chemical composition of the coatings were analyzed by X-ray energy-dispersive spectrometry (XEDS) using a VG-HB603 dedicated scanning-transmission electron microscope (STEM), using an electron beam focussed to a 4 nm diameter.

3. Results and discussion

3.1. Coating microstructure

Fig. 1(a) shows a fracture cross-section of a typical adherent and uniform mullite coating on SiC. Fig. 1(b) shows a cross-sectional TEM micrograph of a CVD mullite coating. The pore and crack-free nature of the coating is evident. Fig. 2 shows the X-ray diffractogram of the coating, where all non-substrate peaks match with mullite.

A TEM bright-field micrograph in Fig. 3(a) shows a typical CVD mullite coating in cross-section in a region adjacent to the coating/substrate interface. This figure reveals that the coating actually consists of two distinct layers. The majority of the coating is composed of crystalline grains of columnar morphology. Fig. 3(b) shows a selected-area electron diffraction (SAED) pattern from a crystalline grain, which is consistent with [0 1 0] mullite. This layer is designated hereon as the 'crystalline layer'. The vector $2\mathbf{s}$ between the two superlattice reflections around the {1 0 1/2} position is inversely related to the average spacing of anti-phase domain boundaries that form due to the occurrence of long-range 2-D composition modulations in the mullite structure [14].

There appears to be a thin non-crystalline layer below the columnar crystalline layer in Fig. 3(a). High-resolution TEM showed that the lower layer is composed of very fine (~5 nm diameter) crystalline particles embedded in a vitreous matrix. These crystallites are identified as γ-Al_2O_3 from the SAED pattern from this region, shown in Fig. 3(c). Thus, this lower layer is designated hereon as the 'nano-

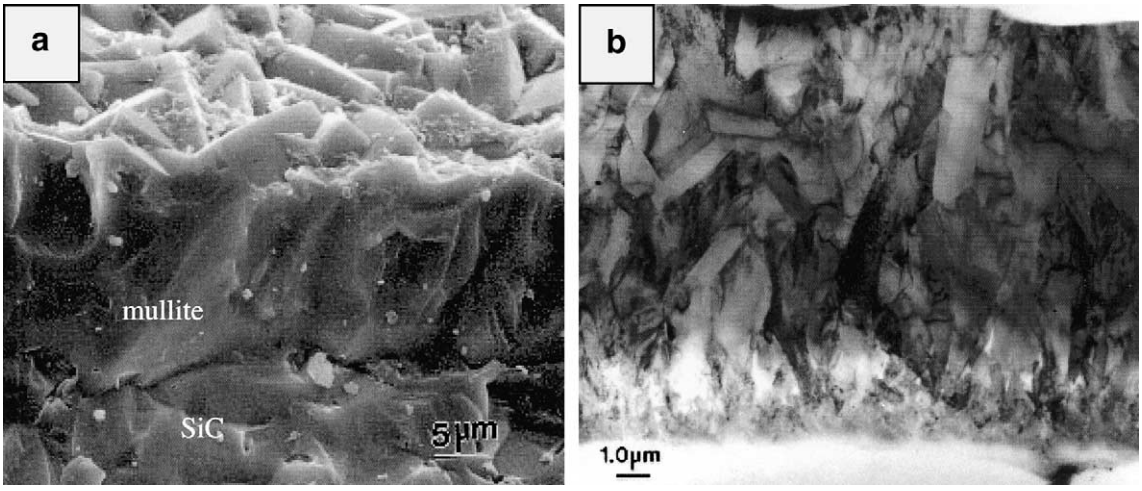

Fig. 1. (a) SEM micrograph of a fracture cross-section of a uniform and adherent CVD mullite coating on SiC. (b) TEM micrograph of the dense mullite coating in cross-section.

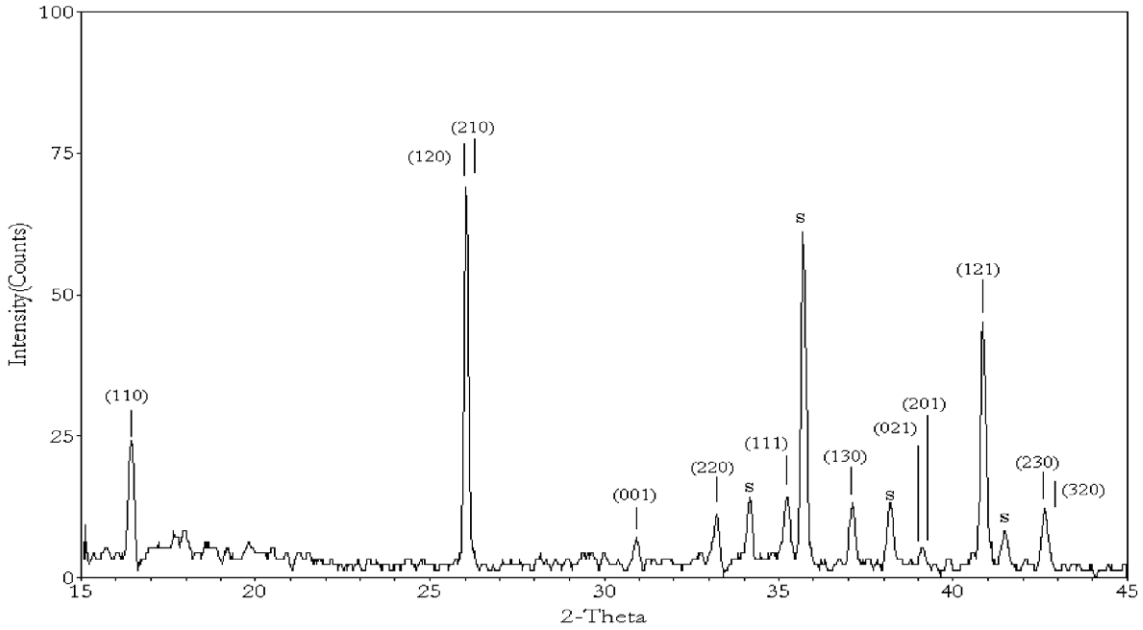

Fig. 2. X-ray diffractogram of a CVD mullite coating. The substrate (SiC) peaks are marked as S. All non-substrate peaks are indexed as mullite. The tetragonal structure of the as-deposited mullite coating is evident by the lack of splitting of the 120/210 peaks.

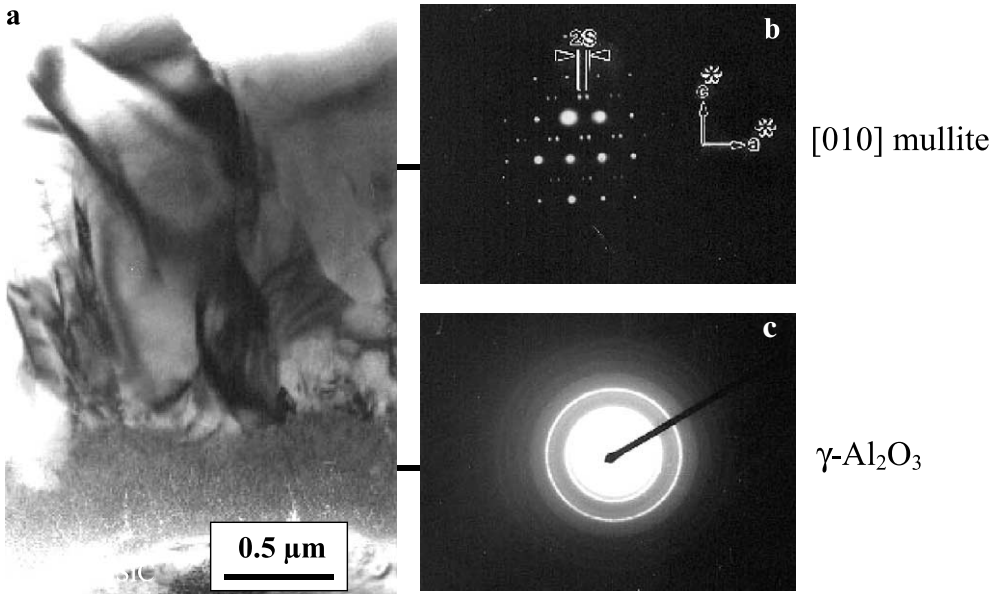

Fig. 3. (a) Cross-section TEM micrograph close to the coating/substrate interface, showing that the coating starts off as a nanocrystalline layer, before crystalline mullite grains nucleate. (b) [010] SAED diffraction pattern from a mullite grain in the coating. (c) SAED pattern from the nanocrystalline layer, showing the ring pattern from the γ-Al_2O_3 nanocrystallites.

crystalline layer'. The above described microstructure of a nanocrystalline layer at the coating/substrate interface, with a layer of crystalline mullite grains over the nanocrystalline layer was typical for all coatings grown on SiC substrates under the deposition conditions used in this study [15].

3.2. Composition gradation

The composition of the mullite coatings was graded from being silica-rich close to the coating/substrate interface to being alumina-rich towards the outer surface of the coating. Fig. 4 shows the composition profile

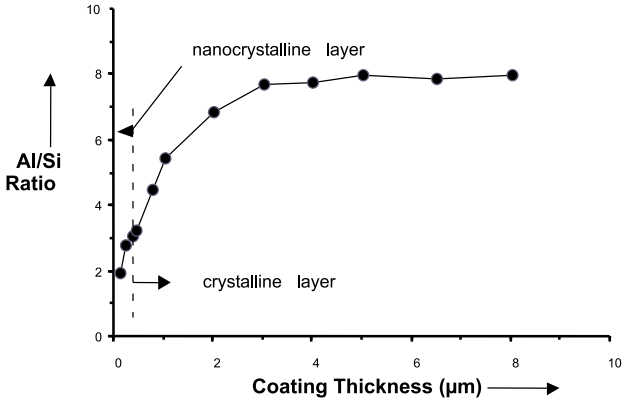

Fig. 4. Gradation of the composition across the coating thickness, expressed as an Al/Si ratio. The interface between the nanocrystalline and crystalline layers occur close to the stoichiometric Al/Si ratio of 3.

across a typical coating. The composition is plotted as the Al/Si ratio, whose value is 3 in stoichiometric mullite. Interestingly, the mullite grains nucleated when the Al/Si ratio in the nanocrystalline layer was $\sim 3.2 \pm 0.3$ [16], which is close to that of stoichiometric mullite. Once nucleated, the mullite grains could be made to grow over a wide range of non-stoichiometric Al-rich compositions. Fig. 4 shows that the surface of the mullite coating was highly alumina-rich (Al/Si $\sim$ 8). By suitable manipulation of the input $AlCl_3/SiCl_4$ ratio, Al/Si ratios as high as 15 have been achieved at the coating surface. These compositions are among the most alumina-rich mullite reported to-date in the literature [17]. There is a strong practical motivation to substantially reduce or even virtually eliminate the silica component from the coating surface, which is in direct contact with corrosive atmospheres containing steam.

To understand how mullite can accommodate such a wide range of Al/Si ratio, the crystal structure of mullite needs to be examined. Mullite, with a space group of Pbam (space group number 55), is a derivative structure of sillimanite ($Al_2O_3 \cdot SiO_2$) [18]. Fig. 5(a) shows the [0 0 1] projection of the sillimanite structure, in which chains of AlO_6 octahedra are aligned parallel to the *c*-axis. These chains are linked by double chains of AlO_4 and SiO_4 tetrahedra that are arranged in an ordered sequence along the *c*-axis. Mullite is derived from sillimanite by substituting Al^{3+} ions for Si^{4+} in the tetrahedral positions and removing oxygen atoms to balance the electric charge. As shown in Fig. 5(b), the formation of an oxygen vacancy causes the two cations (Si, Al) in the tetrahedral positions (T) to shift to the neighboring tetrahedral position (T*). Correspondingly, an oxygen atom adjusts its position from O_c to O_{c^*}, leading to a reduction in symmetry [19]. The average crystal structure of stoichiometric mullite is orthorhombic in which edge-sharing AlO_6 octahedral chains are cross-linked by (Si, Al)O_4 tetrahedra arranged in a random fashion

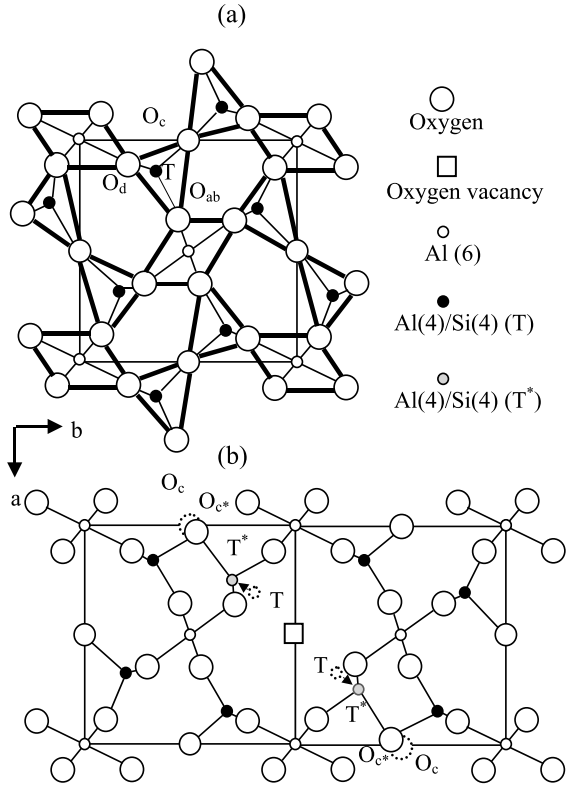

Fig. 5. (a) [0 0 1] projection of the unit cell of sillimanite. (b) Structure of mullite, shown as a derivative structure of silimanite, where the substitution of Si^{4+} with Al^{3+} leads to the formation of oxygen vacancies and an accompanying movement of cations from the T to the T* sites [19].

along the *c*-axis. Due to the disordering of these (Si, Al)O_4 tetrahedral sites, the *c* lattice parameter of mullite is half the *c* lattice parameter of sillimanite [20].

3.3. High-temperature stability

To study the high-temperature stability of the coatings, annealing studies were carried out in a temperature range 1000–1400 °C, with typical annealing times of 100 h. Fig. 6 shows the composition profiles across a mullite coating in the as-deposited state and after a 100 h anneal at 1250 °C. The figure shows that there is a little variation in the coating composition profile as the result of the anneal. This shows that long-range-diffusion processes are not occurring in the coating, indicating that mullite is a good diffusion barrier.

As discussed, stoichiometric mullite has an orthorhombic structure ($a = 7.5456$ Å, $b = 7.6895$ Å, $c = 2.8842$ Å). Since the lattice parameters, *a* and *b*, are slightly different, there is typically a splitting of 120/210, 230/320, 240/420, 041/401, and 250/520 peak pairs in the XRD diffractogram of mullite. However, X-ray diffractogram of as-deposited mullite coatings (see Figs. 2 and

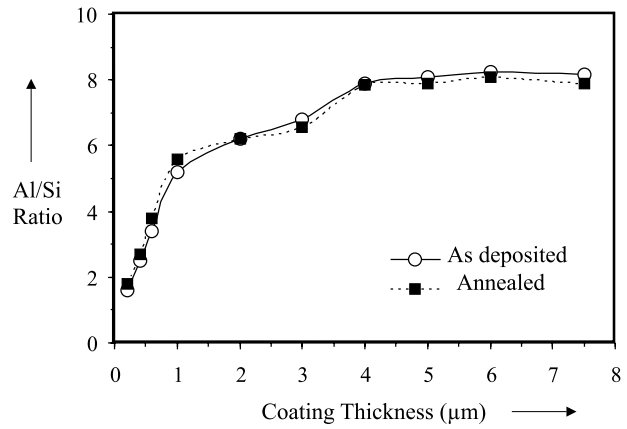

Fig. 6. (a) Composition profiles across a graded mullite coating in the as-deposited state and after a 100 h anneal at 1250 °C.

7(a)) almost never exhibit a splitting of such pairs, indicating that the as-deposited mullite coatings have a tetragonal structure (equal a and b lattice parameters) [14]. Annealing the as-deposited coatings for 100 h at temperatures of 1200 °C and above led to a tetragonal-to-orthorhombic transformation, with the splitting of the peak pairs becoming more evident at higher temperatures. Fig. 7(b) shows a clear splitting of the 120/210 peak pair after a 100 h anneal at 1250 °C. The lack of compositional changes on annealing (Fig. 6) suggests that the tetragonal-to-orthorhombic transformation occurred by some short-range structural readjustment.

To understand the origins of the tetragonal-to-orthorhombic transformation, the derivative structures of sillimanite needs to be examined. All sillimanite derivative structures have tetrahedrally coordinated Al and Si atoms that can occupy either T or T* sites [21]. Fig. 7(c) shows that there are four sites of each kind (T and T*) in the unit cell of mullite. Preferential occupation of T sites makes the lattice parameter a smaller than b. Examples of such structures include sillimanite, where the occupancy of T sites, O_T, is 1 and the occupancy of T* sites, O_{T^*}, is 0, leading to $a = 7.470$ Å and $b = 7.663$ Å; and mullite, where $O_T = 0.863$ and $O_{T^*} = 0.137$, leading to $a = 7.5456$ Å and $b = 7.6895$ Å. Conversely, preferential occupation of T* sites makes the lattice parameter a larger than b, as in andalusite ($Al_2O_3 \cdot SiO_2$) [22].

In CVD mullite deposition, coatings were deposited at relatively high growth rates (~5 μm/h) and low temperatures (~950 °C). Lacking sufficient time and surface mobility, the AlO_4 and SiO_4 tetrahedra populate the T and T* sites randomly, leading to the metastable tetragonal structure in the as-deposited coatings. When annealed at elevated temperatures, the tetrahedra undergo local readjustment to thermodynamically favorable positions, leading to an asymmetric occupation of T and T* sites, causing the tetragonal-to-orthorhombic

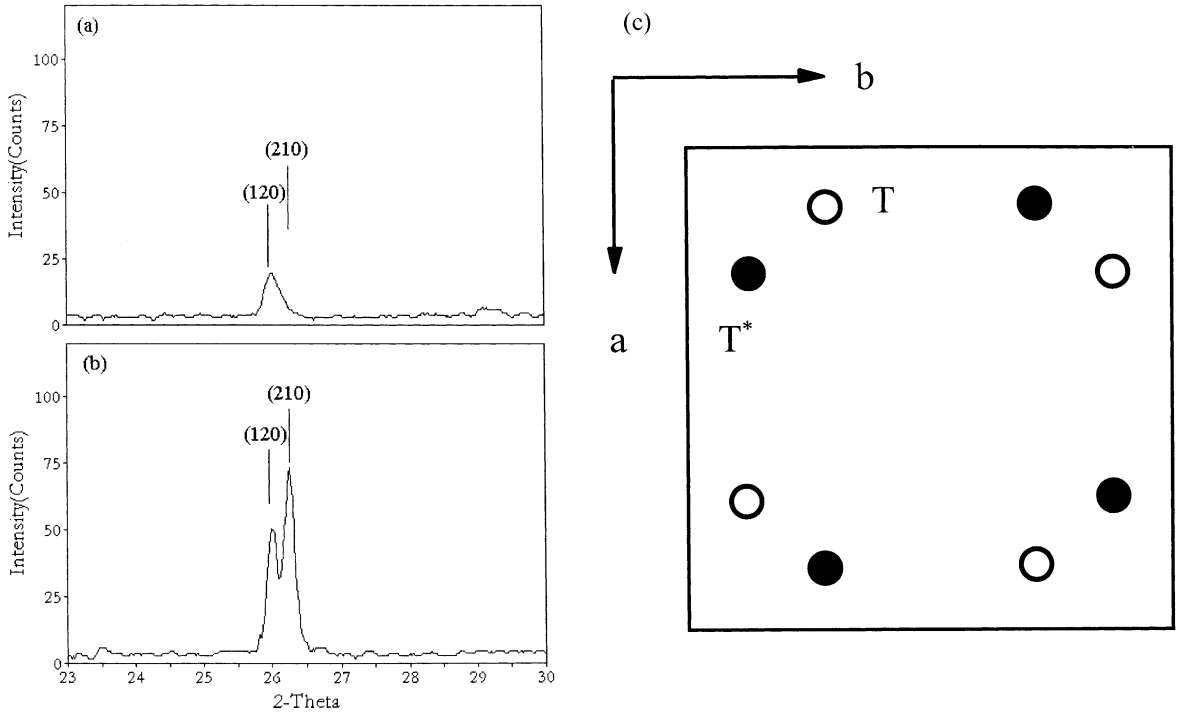

Fig. 7. (a) Lack of splitting of the 120/210 pair of mullite, showing a tetragonal structure. (b) Evidence of tetragonal-to-orthorhombic transformation due to a 100 h anneal at 1250 °C due to the presence of a 120/210 peak split. (c) Schematic of the 4 T and 4 T* sites in sillimanite stuctural derivatives [21].

transformation. Higher annealing temperatures increase the atomic mobility, leading to more defined splitting of the 120/210 pairs. In fact, the mullite structure can move towards a tetragonal configuration due to composition effects alone. In high-Al mullite, increasing the Al content produces oxygen vacancies in the O_c sites and moves Al/Si atoms from T to T* sites. This increases the relative occupancy of T* sites and leads to an increase in the *a* lattice parameter and a decrease in the *b* lattice parameter with increasing Al content. Studies have shown that the mullite structure becomes tetragonal at 78 mol% alumina (Al/Si $\sim$ 7) [23]. However, for the CVD mullite, the as-deposited coatings were tetragonal even when the maximum composition was well below this value, indicating that the tetragonality is not solely composition driven.

On annealing for 100 h at temperatures of 1150 °C and above, phase transformations were observed in the nanocrystalline layer of the mullite coatings. The nature of the phase transformation depended on the input $AlCl_3/SiCl_4$ gas phase ratio used to deposit the nanocrystalline layer. For nanocrystalline layers deposited using an $AlCl_3/SiCl_4$ input ratio of 2 and greater, the γ-Al_2O_3 nanocrystallites and the vitreous silica-rich matrix always reacted to form crystalline grains after a 100 h anneal in the temperature range 1150–1300 °C. Fig. 8(a) shows a TEM micrograph of a nanocrystalline layer, grown using an input $AlCl_3/SiCl_4$ ratio of 2, after a 100 h anneal at 1300 °C. The figure shows that the entire microstructure has been converted to equiaxed crystalline grains with no accompanying microcracking or porosity formation. The SAED pattern from one such grain, shown in Fig. 8(b), is consistent with [2 1 4] mullite. Thus, the entire nanocrystalline layer (deposited with an input $AlCl_3/SiCl_4$ ratio of 2) was converted to equiaxed mullite grains, whose grain size increased from $\sim$10 nm for the 1150 °C anneal to $\sim$100 nm for the 1300 °C anneal.

In contrast, a nanocrystalline layer deposited using an input $AlCl_3/SiCl_4$ ratio of 1, did not convert completely to mullite on annealing. Fig. 9(a) shows a cross-sectional TEM bright-field micrograph of such a nanocrystalline layer after a 100 h anneal at 1250 °C. The micrograph shows two discernable sublayers. The SAED diffraction pattern from the crystalline bottom layer, shown in Fig. 9(b), is consistent with [$\bar{1}$ 1 1] cristobalite (α-SiO_2). However, a calculation of the interplanar spacings from the SAD pattern showed a 6.4% dilation of the ideal cristobalite structure, likely due to the incorporation of the larger Al^{3+} ions [24]. The HREM micrograph in Fig. 9(c) shows the upper layer to consist of nanosized crystalline mullite grains embedded in a Si-rich vitreous matrix. The SAD pattern from this upper layer did not show the presence of γ-Al_2O_3 nanocrystals, indicating that the γ-Al_2O_3 had dissolved into the vitreous silica-rich matrix on annealing. This observation is consistent with the studies of Wei and Halloran [25,26] on mullitization mechanisms in diphasic sol–gels, which transformed into an intimate mixture of γ-Al_2O_3 and vitreous silica. They reported that the nucleation mechanism consisted of three serial steps, dissolution of γ-Al_2O_3 in the vitreous silica matrix, nucleation of mullite after an incubation period, and growth of mullite grains by diffusion in the matrix phase.

Thus, a nanocrystalline layer grown with an input $AlCl_3/SiCl_4$ ratio of 1 underwent partial mullitization, while nanocrystalline layers grown with an input $AlCl_3/SiCl_4$ ratio of 2 or higher underwent complete mullitization, when annealed at 1250 °C for 100 h. Since the average Al/Si ratio in a nanocrystalline layer increases with increasing input $Al_3/SiCl_4$ ratio, it is concluded that the presence of sufficient Al content in the nanocrystalline layer is necessary to ensure complete mullitization.

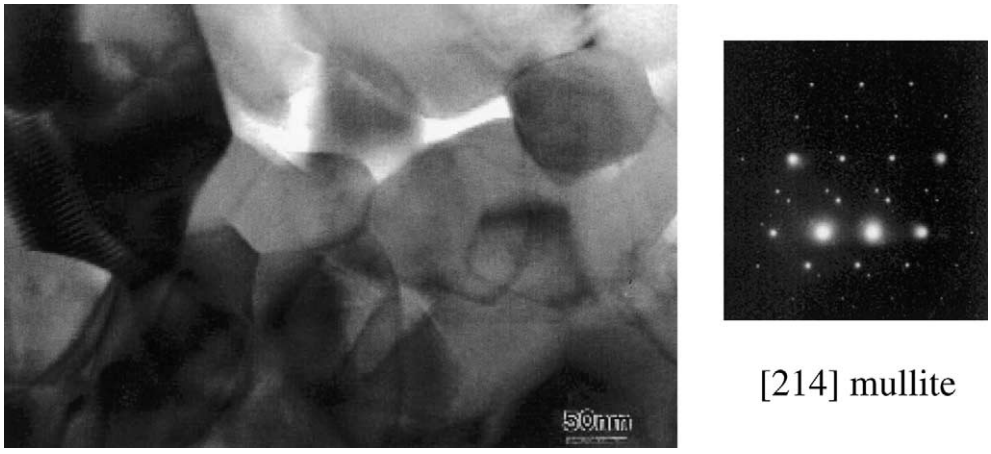

Fig. 8. (a) Complete mullitization of a nanocrystalline layer deposited with an input $AlCl_3/SiCl_4$ ratio of 2, as a result of a 100 h anneal at 1300 °C. (b) [2 1 4] SAED pattern of mullite from one of the equiaxed grains.

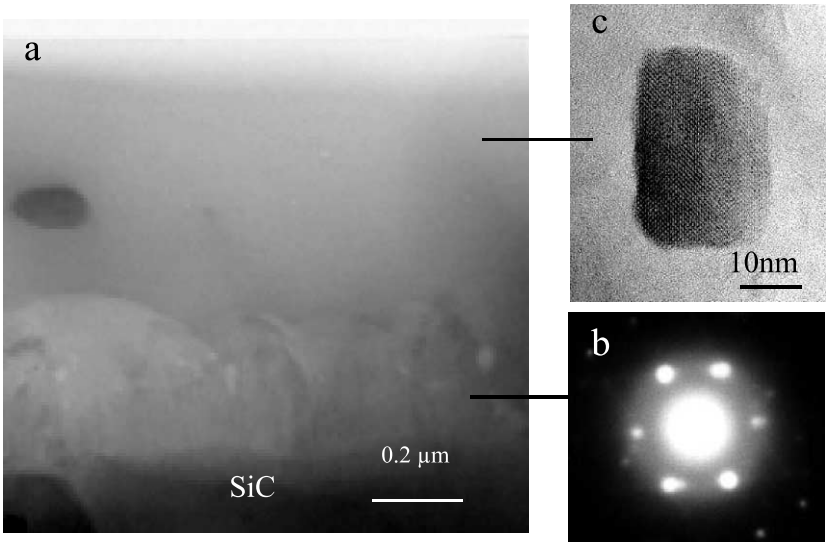

Fig. 9. (a) Cross-sectional TEM micrograph showing two discernable layers formed after a 100 h anneal at 1250 °C in a nanocrystalline layer deposited with an input $AlCl_3/SiCl_4$ ratio of 1. (b) $[\bar{1}\,1\,1]$ SAED pattern of cristobalite from bottom layer, formed by devitrification of silica. (c) High-resolution TEM micrograph of the upper layer, showing the presence of a mullite crystallite in a silica-rich vitreous matrix.

There is a practical need to avoid devitrification of silica in the nanocrystalline layer to cristobalite. The cristobalite phase has a large CTE (10.3×10^{-6} °C^{-1}) mismatch with the SiC substrate (4.7×10^{-6} °C^{-1}). Devitrification of silica has been known to cause spallation of coatings due to the large stresses that accompany a 3.3% volume reduction that occurs when vitreous silica converts to β-cristobalite, and a further 2.2% volume reduction when β-cristobalite transforms to α-cristobalite [27]. In fact, devitrification of the silica to cristobalite is thought to be the primary cause for cracking and spallation of the mullite coatings, when they were annealed at 1400 °C for 100 h. Fig. 10(a) shows the surface of such a coating, while Fig. 10(b) shows the presence of a cristobalite peak in the XRD scan from the coating.

Interestingly, if the coatings were first pre-annealed for 100 h at 1250 °C, the coatings were completely adherent and crack-free after the subsequent 100 h anneal at 1400 °C. Fig. 11(a) shows a low magnification SEM micrograph of the surface of such a coating. A higher magnification micrograph (see Fig. 11(b)) of the coating surface shows an absence of microcracks as well as a lack of any substantial grain growth, even after the 1400 °C exposure. It is conjectured that the complete mullitization of the nanocrystalline layer during the 1250 °C pre-anneal, prevented the devitrification of silica during the 1400 °C anneal. This was supported by the lack of a cristobalite peak in the XRD scan. Thus, pre-treatment of CVD mullite coatings at 1250 °C to induce complete mullitization of the nanocrystalline layer is desired before exposure to temperatures as high as 1400 °C for long-term applications.

The adhesion of the mullite coatings was also tested by cycling the temperature between 1250 °C and room temperature. The samples were subjected to substantial thermal shock by rapid insertion and removal of the samples from the hot zone of the furnace and holding the sample for 1 h at each temperature. Fig. 12(a) shows a fracture cross-section of a coating after 500 cycles. The coating exhibited no signs of cracking and spallation. The excellent adhesion of the coating can be partially attributed to two reasons. The first is the formation of equiaxed mullite grains in the nanocrystalline layer surface leading to a close CTE match at the coating/substrate interface. The second is the gradation of the CTE across the thickness of the mullite coating, which avoids any abrupt changes of CTE across the coating thickness, while allowing the coating surface to be highly alumina-rich.

Interestingly, as seen in the cross-sectional TEM micrograph (Fig. 12(b)), the high-alumina coating surface (Al/Si $\sim$ 8) showed no signs of phase separation after a total of 500 h of exposure at 1250 °C during this cyclic oxidation test. As seen in the XRD plot in Fig. 10(b), annealing an alumina-rich coating at 1400 °C for 100 h led to the formation of corundum (α-Al_2O_3) peaks. To better understand the effect of coating composition on phase separation, a compositionally graded coating (surface Al/Si *ratio* $\sim$ 8) that had been subjected to the two-step anneal (100 h at 1250 °C followed by 100 h at 1400 °C) was carefully examined in the TEM. In general, other than the previously described tetragonal-to-orthorhombic transformation and mullitization of the nanocrystalline layer, no other morphological changes were seen in regions where the Al/Si ratio was below 5.

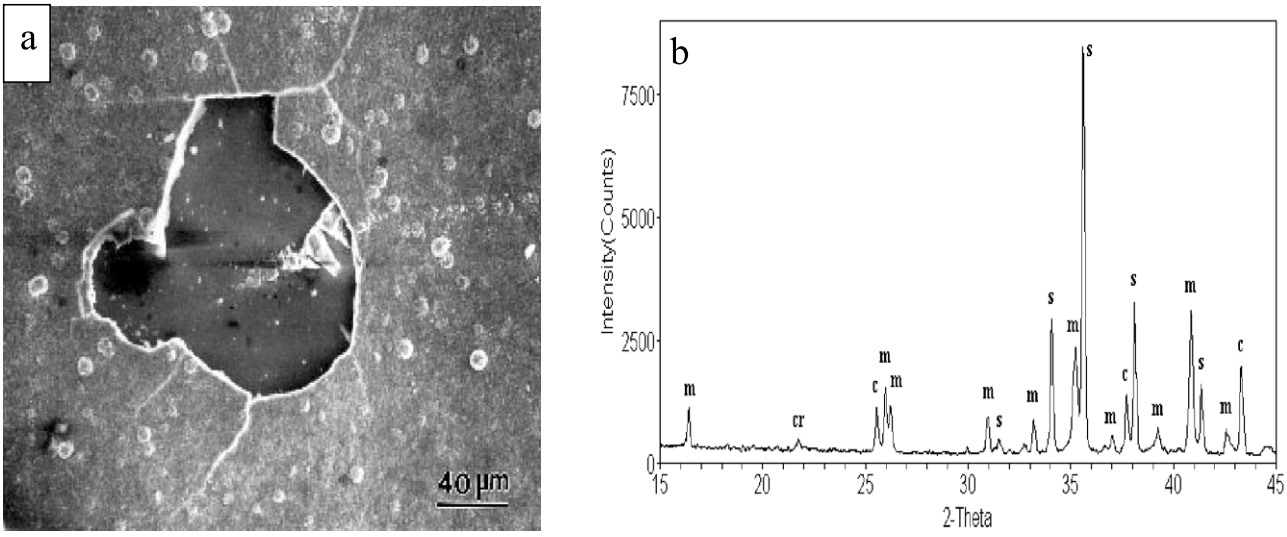

Fig. 10. (a) Cracking and spallation in a CVD mullite coating annealed at 1400 °C for 100 h. (b) XRD diffractogram from coating, showing the presence of cristobalite (cr) and α-Al_2O_3 (corundum) phases (C) in the annealed coating.

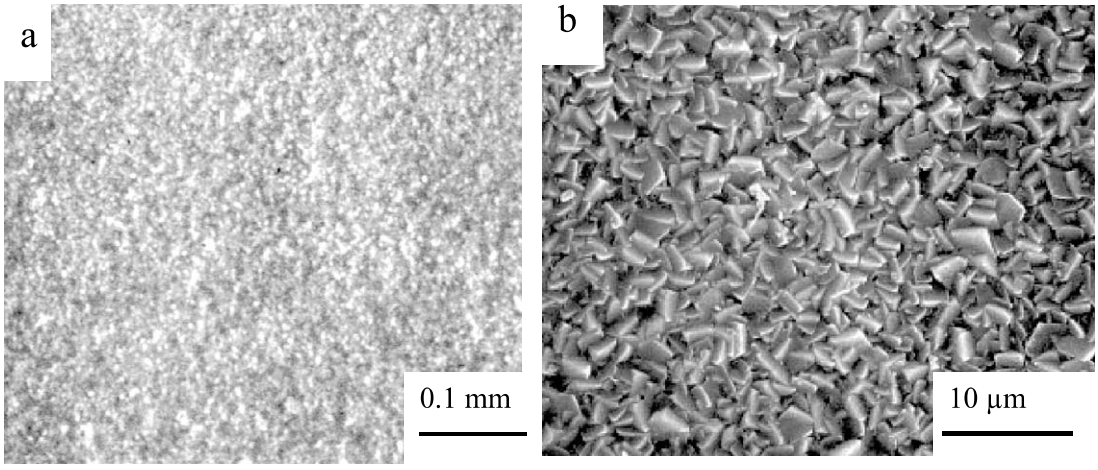

Fig. 11. (a) Low magnification SEM micrograph showing no cracking or spallation in a CVD mullite coating pre-annealed at 1250°for 100 h, followed by a 100 h anneal at 1400 °C. (b) Higher magnification SEM micrograph of coating surface, showing a lack of microcracking and grain growth, even after the 100 h exposure at 1400 °C.

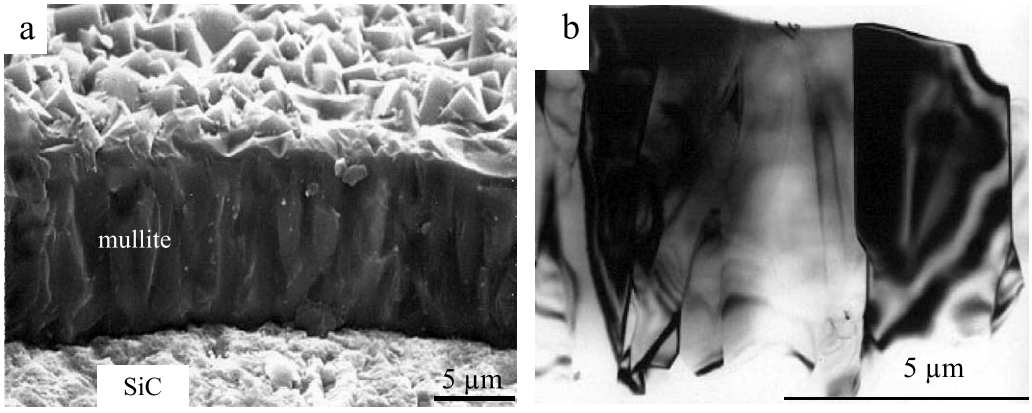

Fig. 12. (a) Fracture cross-section of CVD mullite coating showing excellent adhesion after 500 cycles of cyclic oxidation at 1250 °C. (b) Cross-sectional TEM micrograph showing no phase separation after the 500 h exposure at 1250 °C.

In regions where the Al/Si ratio was between 5 and 6, 100–300 nm sized precipitates were observed, as shown in Fig. 13. It is significant to note that this precipitation phenomenon was not accompanied by the formation of any microcracks. Microanalysis in the STEM showed the Al/Si ratio in these precipitates to be very high (~47), strongly indicating that this was the Al_2O_3 phase responsible for the corundum peaks seen in the XRD pattern (Fig. 10(b)). The precipitation of the corundum phase in Al-rich mullite is consistent with reports by other researchers [17], suggesting that annealing Al-rich CVD mullite may be a viable method of producing uniform finely dispersed Al_2O_3/mullite nanocomposite coatings.

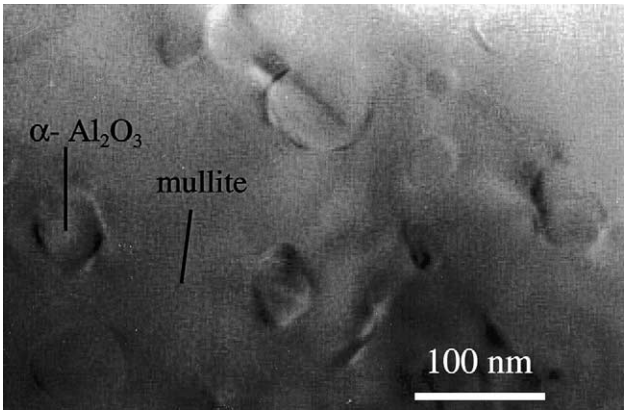

Fig. 13. Crack-free precipitation of nanosized α-Al_2O_3 in the high Al-mullite ($5 < Al/Si < 6$) after the two-step anneal of 100 h at 1250 °C, followed by 100 h at 1400 °C.

At higher Al contents ($6 < Al/Si < 8$), precipitation of α-Al_2O_3 was accompanied by the formation of twins in the mullite matrix. Fig. 14(a) shows the microstructure of a region, where the overall Al/Si ratio was measured as 7.2. In addition to the corundum precipitates, irregular lamellae of twinned mullite, 20–100 nm in width can be seen in the figure. Fig. 14(b) also shows a [0 1 0] SAD pattern from the twinned region. The SAED pattern shows that the twin planes are aligned along (0 0 1), in agreement with the observations of Nakajima and Ribbe [28]. Fig. 14(c), a schematic of the indexed SAED pattern, shows that four superlattice spots appear around the {1 0 1/2} position in the SAED pattern from the twinned region. One pair of the superlattice spots (e1-type) is related to a twin, while the other pair (e2-type) is related to the other twin. In twinned mullite, the 2**s** vector joining the 'e1-type' diffraction spots also has a c^* component that increases with increasing Al/Si ratio in the mullite.

3.4. Corrosion resistance

By dint of the nature of the composition gradation, the CVD mullite coatings on SiC are expected to have the hot-corrosion and recession resistance of alumina coatings, while maintaining the thermal shock resistance of stoichiometric mullite coatings. Mullite-coated and uncoated SiC substrates were subjected to hot-corrosion tests by loading the surface with about 5 mg/cm^2 of Na_2SO_4 and subjecting the samples to flowing oxygen at 1100 °C for 300 h [29]. Fig. 15(a) shows a depth of attack in excess of 20 μm below the uncoated SiC surface.

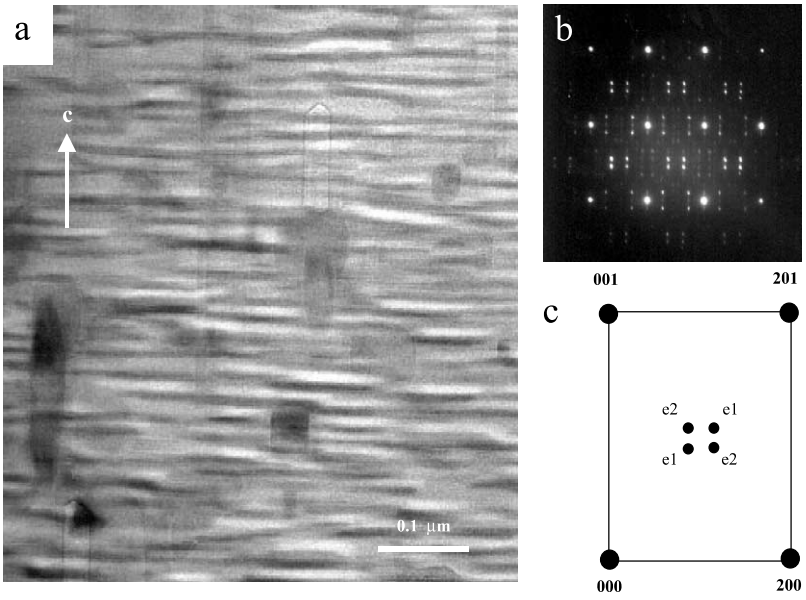

Fig. 14. (a) TEM micrograph showing twin formation in high-Al mullite ($6 < Al/Si < 8$) after the two-step anneal of 100 h at 1250 °C, followed by 100 h at 1400 °C. (b) [0 1 0] SAED pattern of twinned mullite. (c) Schematic of two pairs of superlattice reflections from twinned mullite.

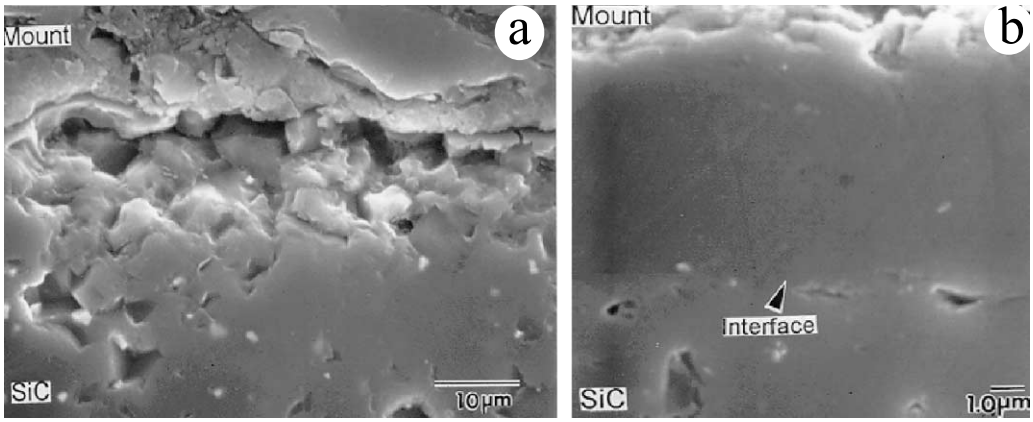

Fig. 15. Hot-corrosion test of: (a) uncoated; (b) CVD mullite-coated SiC substrates. After a 300 h exposure at 1100 °C, the uncoated sample had a 20 μm depth of hot-corrosion attack, while the mullite-coated sample was practically unaffected, indicating the efficacy of CVD mullite coatings as a corrosion barrier for Si-based ceramics.

In direct contrast, the mullite-coated SiC sample exhibited no weight loss. Fig. 15(b) shows the coating in cross-section showing no hot-corrosion attack either within the coating or at the interface, indicating that the mullite coating indeed acted as a very effective hot-corrosion barrier under highly corrosive conditions.

4. Conclusions

Uniform, dense and adherent mullite coatings were deposited on SiC by the CVD process. The coatings were compositionally graded with the Al/Si ratio increasing towards the outer surface of the coating. The coatings started out as a mixture of γ-Al_2O_3 nanocrystallites embedded in a vitreous silica-rich matrix, before mullite grains nucleated at an Al/Si ratio of $\sim$3.2. The as-deposited coatings have a tetragonal structure, which converted to the equilibrium orthorhombic mullite structure on annealing at temperatures of 1200 °C and above. On annealing at temperatures of 1150 °C and above, the nanocrystalline layer was converted to equiaxed crystalline mullite grains. These compositionally graded coatings exhibited excellent adhesion during annealing at temperatures in excess of 1300 °C. Annealing at 1400 °C, led to cracking and spallation of the coating due to devitrification of silica to cristobalite in the nanocrystalline region. However, this phenomenon could be effectively prevented by pre-annealing the coating at 1250 °C to completely mullitize the nanocrystalline layer, thus effectively preventing the devitrification of silica during the 1400 °C anneal. In addition, at this elevated temperature, precipitation of α-Al_2O_3 and twinning occurred in regions of progressively increasing Al/Si ratio, without any accompanying microcracking. The highly alumina-rich outer surface made CVD mullite coatings highly effective corrosion barriers.

Acknowledgements

This research was partially supported by the US Department of Energy as part of the Ceramics Technology Project of the Propulsion System Materials Program and the Fossil Energy AR and TD Materials Program with Martin Marietta Energy Systems, Inc. The authors would like to acknowledge contributions by Dr. Michael Auger, Dr. Arun Pattanaik and Dr. Rao Mulpuri. The electron microscopy studies were carried out at the Center for Electron Microscopy at MIT.

References

[1] Matsui M. Status of research and development on materials for ceramics gas turbines components. In: Chen I-W, Becher PF, Mitomo M, Petzow G, Yen T-S, editors. Silicon nitride ceramics, scientific and technology advances, Symposium Proceedings, vol. 287. Materials Research Society; 1993. p. 173–88.

[2] DiMascio PS, Orenstein RM, Rajiyah H. Reliability of a conceptual ceramics gas turbine component subjected to static and transient thermomechanical loading. J Eng Gas Turbines Power 1998;120(2):263–70.

[3] Wereszczak AA, Kirkland TP. Creep performance of candidate SiC and Si_3N_4 materials for land-based, gas turbine engine components. J Eng Gas Turbines Power 1997;119:799–806.

[4] Yang S, Gibson RF, Crosbie GM, Allor RL. Thermal cycling effects on dynamic mechanical properties and crystallographic structures of silicon nitride-based structure ceramics. J Eng Gas Turbines Power 1997;119:279–84.

[5] Luthra KL. Some new perspectives on oxidation of silicon carbide and silicon nitride. J Am Ceram Soc 1991;74:1095–103.

[6] Jacobson NS. Corrosion of silicon-based ceramics in combustion environment. J Am Ceram Soc 1993;76(1):3–28.

[7] Hsu PP, Ip S, Park C, McNallan MJ. Oxidation of silicon, silicon carbide, and silicon nitride in gases containing oxygen and chlorine. J Am Ceram Soc 1993;76(6):1621–3.

[8] Robinson RC, Smialek JL. SiC recession caused by SiO_2 scale volatility under combustion conditions: I, Experimental results and empirical model. J Am Ceram Soc 1999;82(7):1817–27.

[9] Jacobson NS, Smialek JL. Hot corrosion of sintered α-SiC at 1000 °C. J Am Ceram Soc 1985;68(8):432–9.
[10] DeKaiser WL. Science of ceramics, vol. II. New York: Academic Press; 1963.
[11] Lee N, Miller RA. Long-term durability of mullite-coated silicon-based ceramics. Ceram Eng Sci Proc 1994;15(4):547–54.
[12] Sarin VK, Mulpuri RP. Chemical vapor deposition of mullite coatings. US Patent No. 576008, 1998.
[13] Mulpuri RP, Sarin VK. Synthesis of mullite coatings by chemical vapor deposition. J Mater Res 1996;11(6):1315–24.
[14] Doppalapudi D, Basu SN. Structure of mullite coatings grown by chemical vapor deposition. Mater Sci Eng 1997;A231:48–54.
[15] Basu SN, Hou P, Sarin VK. Formation of mullite coatings on silicon based ceramics by chemical vapor deposition. J Refractory Metals Hard Mater 1999;16(4–6):343–52.
[16] Hou P, Basu SN, Sarin VK. Nucleation mechanisms in chemically vapor-deposited mullite coatings on SiC. J Mater Res 1999; 14(7):2952–8.
[17] Fischer RX, Schneider H, Voll D. Formation of aluminum rich 9:1 mullite and its transformation to low aluminum mullite upon heating. J Eur Ceram Soc 1996;16:109–13.
[18] Burnham CW. Crystal structure of mullite. Carnegie Institution Washington Year Book 1963;62:158–62.
[19] Epicier T. Benefits of high-resolution electron microscopy for the structural characterization of mullites. J Am Ceram Soc 1991; 74(10):2359–66.
[20] Cameron WE. Mullite: a substituted alumina. Am Mineral 1977;62:747–55.
[21] Sadanaga R, Tokonami M, Takeuchi Y. The structure of mullite, $2Al_2O_3SiO_2$ and relationship with the structure of sillimanite and andalusite. Acta Crystallographica 1962;15:65–8.
[22] Schneider H, Okada K, Pask JA. Mullite and mullite ceramics. Chichester: Wiley; 1994.
[23] Schneider H, Rymon-Lipinski T. Occurrence of pseudotetragonal mullite. J Am Ceram Soc 1988;71(3):C162–4.
[24] Buerger MJ. Stuffed derivatives of the silica structures. Am Mineral 1954;39(7–8):600–14.
[25] Wei WC, Halloran JW. Transformation kinetics of diphasic aluminosilicate gels. J Am Ceram Soc 1988;71(7):581–7.
[26] Wei WC, Halloran JW. Phase transformation of diphasic aluminosilicate gels. J Am Ceram Soc 1988;71(3):166–72.
[27] Lynch JF, editor. Engineering property data on selected ceramics volume III, single oxides. Metals and Ceramics Information Center Report MCIC-HB-07. Columbus, OH: Battelle Columbus Laboratories; 1981.
[28] Nakajima Y, Ribbe PH. Twinning and superstructure of Al-rich mullite. Am Mineral 1981;66:142–7.
[29] A.K. Pattanaik, V.K. Sarin, High temperature oxidation and corrosion of CVD mullite coated SiC. In: Sudarshan TS, Khor TA, Jeandin M, editors. Surface modification technologies XII. Materials Park, OH: ASM International; 1998. p. 91–8.